Materials Science & Engineering A 962 (2026) 150103

Contents lists available at ScienceDirect

Materials Science & Engineering A

journal homepage: www.elsevier.com/locate/msea

Engineering precipitates via novel hybrid additive manufacturing enables effective hydrogen trapping

Mahdieh Safyari [a,b,*], Michael K. Eusterholz [c,d], Masoud Moshtaghi [a,**]

[a] Mechanics of Materials Lab, Department of Mechanical Engineering, School of Energy Systems, LUT University, P.O. Box 20, Lappeenranta, 53851, Finland
[b] Materials Science and Environmental Engineering, Faculty of Engineering and Natural Sciences, Tampere University, Tampere, Finland
[c] Institute for Applied Materials (IAM-WK), Karlsruhe Institute of Technology (KIT), Kaiserstraße 12, 76131, Karlsruhe, Germany
[d] Karlsruhe Nano Micro Facility (KNMFi), Karlsruhe Institute of Technology (KIT), Hermann-von-Helmholtz-Platz 1, 76344, Eggenstein-Leopoldshafen, Germany

ARTICLE INFO

Keywords:
Wire arc additive manufacturing
Excessive vacancies
Non-equilibrium processing
Hydrogen trapping
Hybrid additive manufacturing

ABSTRACT

This work shows that novel manufacturing routes combining wire arc additive manufacturing (WAAM) and in situ deformation enable control of size, shape, and particle/matrix interface characteristics. To this end, precipitation of the Al_3Sc phase in aluminum alloys was studied in specimens fabricated by as-built (W), as-built and thermally post-processed WAAM, as well as in specimens produced by WAAM combined with in-process rolling (HR-W). The experimentally determined equilibrium shape of Al_3Sc precipitates in HR-W specimens is a large, elongated ellipsoid with coherent interfaces, a morphology not previously reported for this phase. No Al_3Sc particles were detected in W specimens, whereas P-W specimens exhibited the conventional rhombicuboctahedral precipitates with semi-coherent interfaces. Theoretical calculations, together with positron annihilation spectroscopy, confirm that excess vacancies drive this morphological transition. The combination of atom probe tomography, density functional theory, and thermal desorption spectroscopy revealed that coherent $Al_3Sc\|Al$ interfaces trap H, whereas a semi-coherent boundary does not trap hydrogen. These findings highlight the interplay between non-equilibrium processing, defect dynamics, and hydrogen trapping, offering a more fundamental understanding of hydrogen behavior in aluminum alloys.

1. Introduction

The growing demand for lightweight structures in hydrogen technologies calls for high-strength aluminum alloys that can maintain mechanical integrity in hydrogen-rich environments [1–4]. At the same time, there is increasing pressure to reduce energy consumption, material waste, and overall production costs. Metal additive manufacturing (AM) has emerged as a promising solution by enabling the fabrication of components with complex geometries, previously unachievable by conventional methods, without compromising material efficiency [5–7]. These capabilities are particularly valuable in hydrogen-related applications, where optimized designs can reduce weight, enhance functionality, and improve system-level performance [8].

During AM, the material undergoes repeated thermal cycling and solid-state transformations. The resulting microstructure is highly sensitive to the cooling rate, which is, in turn, governed by the specific AM technique and process parameters [9,10]. Recently, several studies have focused on taking advantage of in-process heat treatments during AM to eliminate post-processing steps. This approach allows for the intentional redesign of nanoprecipitates, grain boundary structures, and nanoscale chemical distributions during the build [11–13]. For example, AM of Al–Mg alloys has been shown to increase the solid solubility of alloying elements due to rapid solidification and the associated lattice expansion. The high cooling rates suppress equilibrium phase formation and allow greater retention of solute atoms within the matrix, which can significantly enhance mechanical and corrosion properties and alter precipitation behavior during subsequent thermal or mechanical treatments [14]. This means that by in situ controlling the microstructure, the process becomes more efficient, while also enabling the production of high-performance components with tailored microstructures.

A major microstructural limitation in additively manufactured metals is the formation of columnar grains, which result from directional

---

* Corresponding author. Mechanics of Materials Lab, Department of Mechanical Engineering, School of Energy Systems, LUT University, P.O. Box 20, Lappeenranta, 53851, Finland.
** Corresponding author.
E-mail addresses: mahdieh.safyari@tuni.fi (M. Safyari), masoud.moshtaghi@lut.fi (M. Moshtaghi).

https://doi.org/10.1016/j.msea.2026.150103
Received 11 December 2025; Received in revised form 21 February 2026; Accepted 12 March 2026

solidification and cause anisotropic properties and reduced resistance to cracking [15–18]. These grains typically extend across multiple layers, limiting grain boundary area and leading to poor mechanical performance in directions perpendicular to the build [19]. To address this, high-pressure rolling during or immediately after deposition has been recently explored as an effective method to refine grain structure, fragment columnar grains, and stimulate dynamic recrystallization, promoting the formation of fine, equiaxed grains and enhancing overall structural integrity [20,21]. Another effective strategy involves the addition of grain-refining solute elements such as scandium (Sc), which promote the formation of stable primary particles and inhibit columnar grain growth by acting as heterogeneous nucleation sites during solidification. Ren et al. [22] demonstrated that during WAAM, at Sc contents below 0.15%, Sc was fully dissolved in the Al matrix without inducing grain refinement, resulting in only a slight improvement in mechanical properties. However, at a Sc content of 0.3%, the primary Al_3Sc phase precipitated in the as-deposited material, leading to a notable change in microstructure, significant grain refinement, and marked improvements in mechanical performance. After heat treatment at 350 °C for 1 h, further grain boundary refinement occurred, accompanied by the precipitation of the secondary Al_3Sc phase.

While several studies have demonstrated that high-pressure rolling effectively alters microstructural defects in wrought aluminum alloys [23–27], affecting the kinetics of precipitation during thermo-mechanical or heat treatments, there is still a lack of in-depth research on its impact when applied in-process during the additive manufacturing of these alloys. Therefore, this study aims to investigate the combined effect of Sc addition and in-process high-temperature rolling on the precipitation kinetics and morphology of Al_3Sc particles in aluminum alloys produced by wire arc additive manufacturing (WAAM). A comparative analysis will be conducted among specimens fabricated via (i) standard WAAM, (ii) WAAM followed by post-processing heat treatment, and (iii) WAAM combined with high-pressure in-process rolling. Advanced characterization techniques, including atom probe tomography and high-resolution electron microscopy, will be employed to analyze the distribution, size, and shape of the precipitates. Special attention will be given to understanding the underlying mechanisms responsible for the formation of uniquely shaped Al_3Sc particles in the specimen produced by WAAM combined with in-process rolling.

Subsequently, we investigated the hydrogen trapping behavior of the Al_3Sc particles by directly observing the distribution of hydrogen isotope within these precipitates. This analysis was motivated by previous studies suggesting that dispersoids can act as effective hydrogen traps in metallic systems [28,29]. Hydrogen traps are typically categorized as reversible or irreversible based on their binding energies with hydrogen atoms [30–33]. To evaluate this, thermal desorption spectroscopy (TDS) and density functional theory (DFT) calculations provided insights into the hydrogen binding energy and revealing the atomic-level mechanisms of hydrogen trapping inside these particles. Together, these techniques provided a comprehensive understanding of their role in hydrogen trapping.

2. Experimental procedure

2.1. Materials and processing

Two cuboid Al-Mg-Sc alloy components were fabricated using a multi-pass, multi-layer approach via two processing routes: (i) a hybrid method combining rolling and WAAM (HR-W), and (ii) standard WAAM. Fig. 1 illustrates the single-pass, multi-layer deposition process employed in the hybrid robotic WAAM system. As can be seen in Fig. 1, a roller, positioned immediately after the arc source, is ordered to continuously roll the surface of the newly deposited layer. In both processing routes, a 1.2 mm diameter Al-Mg filler wire was employed, with its chemical composition provided in Table 1. The Mg content in this alloy was selected below the maximum solubility limit in the Al matrix (1.5 wt% in room temperature) to prevent the formation of the β (Al_3Mg_2) phase [34]. Therefore, no second phase particles can be seen in SEM images of the specimens in Fig. 1. An inert gas (95% Ar + 5% CO_2) atmosphere protects the process while the welding arc melts the feed wire, allowing for layer-by-layer metal deposition. Heat flows from the freshly deposited top layer down to the substrate plate. The substrate material was a wrought Al-Mg aluminum alloy plate with dimensions of 250 mm × 200 mm × 20 mm. Building upon a standard WAAM setup, the HR-W system incorporates a rolling device and integrated control software to enhance the process.

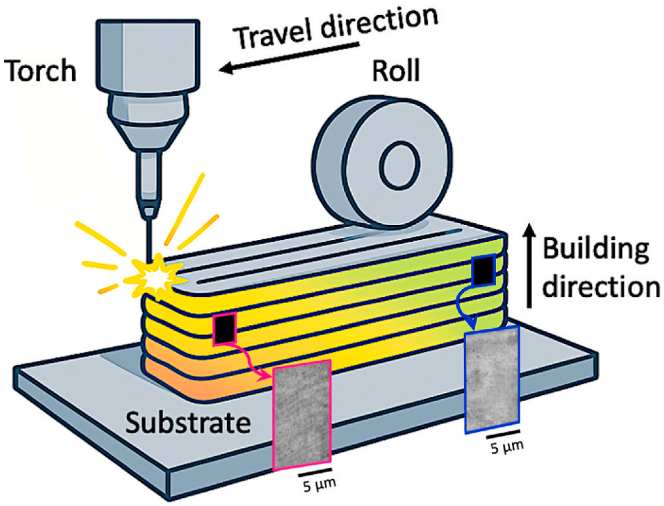

Fig. 1. Schematic of the single-pass, multi-layer deposition and rolling process used in the hybrid robotic additive manufacturing system.

Table 1
Chemical compositions of welding wire and substrate (mass fraction%).

Alloys	Mg	Sc	Mn	Fe	Si	Zn	Al
AlMgSc wire	1.33	0.31	0.22	0.16	0.14	0.05	Balance
Al-Mg substrate	5.91	0.01	0.34	0.30	0.23	0.05	Balance

The HR-W process involves three main forming stages: melting, solidification, and rolling. During the deposition of each new layer, an infrared sensor monitors the alloy's temperature to ensure it remains within the optimal range of 400 ± 5 °C before rolling. The detailed manufacturing parameters used in the processes are provided in Table 2. After preparing the components, three different types of specimens were obtained for further investigation: (i) an as-built WAAM specimen (hereafter W), (ii) a post-processed WAAM specimen subjected to heat treatment at 300 ± 5 °C for 2 h (hereafter P-W), and (iii) an as-built specimen produced by HR-W processing route (hereafter HR-W).

Table 2
Manufacturing parameters of WAAM and HR-W processes.

Mode of Operation	Constant Current mode
Voltage (V)	28
Current (A)	200
Welding speed (mm/min)	700
Wire feed speed (m/min)	4.5
Welding penetration (mm)	1
The overlapping ratio between adjacent welding beads	25%
Rolling reduction in thickness	30%
Shielding gas	95% Ar + 5% CO_2
Shielding gas flow rate (L/min)	18
Nozzle to plate distance (mm)	12.1

2.2. Characterization of second-phase particles

To analyze the microstructure of these specimens at the atomic scale, atom probe tomography (APT) was performed. To avoid Ga contamination, APT samples were prepared by electropolishing with a 20 V voltage in 20 % perchloric acid (70-72 %) in acetic acid (100 %). In a second polishing step, 2 % perchloric acid in butoxyethanol was used. APT analysis was performed with a LEAP 4000X HR instrument (Cameca Instruments, Madison, WI, USA) at 30 K, at a detection rate of 0.3 %, and with a laser wavelength of 355 nm at a pulse energy of 30 pJ and a pulse rate of 100 kHz. APT reconstruction and data evaluation were performed with AP Suite 6.3 (Cameca).

High resolution transmission electron microscopy (HR-TEM) and TEM samples were initially ground to a thickness of approximately 200 μm, followed by jet polishing using a Twin-Jet Polisher with a solution of 25% nitric acid and 75% methanol at −30 °C and an applied voltage of ~8 V. After perforation, the thin foils were further thinned using a low-energy ion mill operated at 500 V. To mitigate knock-off damage during observation, an amorphous protective film (~2 nm thick) was deposited on the reverse side of the foil. Details about the observation of the precipitates can be found in our previous publication [28,35].

Differential scanning calorimetry (DSC) was performed with a Netzsch DSC 204 F1 Phoenix. Each run covered 50 °C to 450 °C at a constant heating rate of 10 K min^{-1}. Circular specimens (Ø 4.8 mm) were punched from the test alloy, and matching discs of high-purity aluminum were prepared as the reference. Positrons were generated from a 0.5 $MBq^{22}Na$ source, encapsulated in Kapton foil and sandwiched between two identical alloy specimens (10 × 10 × 1 mm^3). After entering the alloy, the positrons annihilated and emitted characteristic 511 keV γ-rays. A fast-timing system correlated each annihilation pulse with the β^+-decay start signal, yielding individual lifetimes. Approximately 10^5 events were accumulated per spectrum. Measurements began either immediately after the HR-W process or after brief artificial ageing, followed by ~1s of handling at 300 ± 5 °C. All experiments in this study were performed at least three times to ensure reliability and reproducibility, and all specimens were carefully selected from the center of each component.

2.3. Hydrogen interaction with second-phase particles

For hydrogen mapping, specimens were electrochemically hydrogen-charged for 48 h in a 3.5 wt% NaCl solution at a constant current density of 10 mA cm^{-2}. Immediately after charging, they were kept in liquid nitrogen to minimize hydrogen loss. TDS was then conducted, recording the hydrogen partial pressure while the temperature was ramped at 300 °C h^{-1}.

To investigate hydrogen trapping behavior at coherent Al_3Sc precipitate interfaces, first-principles calculations based on DFT were performed using the Vienna Ab initio Simulation Package (VASP). A bilayer model comprising eight (001) atomic planes of face-centered cubic (f.c.c.) Al and eight (001) planes of Al_3Sc was constructed to simulate a coherent $(001)Al\|(001)Al_3Sc$ interface. The interface was modeled in a cube-on-cube orientation to replicate a fully coherent configuration. Hydrogen atoms were systematically inserted into all non-equivalent tetrahedral interstitial sites at incremental distances from the interface mid-plane. For each configuration, atomic positions were fully relaxed until the forces on each atom were below 0.01 eV/Å.

To assess the solution energy (ΔE_s) of hydrogen at these sites, the total energy of the relaxed hydrogen-containing system was compared with that of the pristine system and an isolated hydrogen atom. The hydrostatic strain field induced by the coherent lattice match was also evaluated. The same methodology was applied to a second model where the precipitate exceeded its critical radius and lost coherency. This was achieved by introducing a periodic array of $\langle 110 \rangle$ 60° edge dislocations at the interface to mimic the relaxation of misfit strain. The impact of coherency loss on hydrogen trapping was quantified by calculating the solution energy at interfacial and dislocation core sites. More information can be found in our previously published paper [28].

3. Results

3.1. Characterization of second-phase particles

Fig. 2a presents a bright-field TEM image revealing dense dislocation tangles formed in the W-specimen which was in as-built WAAM condition. These are attributed to the complex thermal cycles inherent to the layer-by-layer deposition process [36]. A high density of dislocations is observed both at grain boundaries and within grain interiors, indicating substantial internal stress and plastic deformation introduced during rapid solidification. The figure also includes corresponding EDS Mg and Sc elemental maps, which show that no secondary phases have precipitated from the aluminum matrix, even in regions with high dislocation density. These findings are consistent with the APT results shown in Fig. 2b and c, which further confirm the absence of significant solute clustering or second-phase precipitation. In particular, the atom pair correlation analysis in Fig. 2c shows that the experimental Sc–Sc distribution closely matches that of a randomized dataset, indicating a homogeneous distribution without clustering or segregation. In a random solid solution, such distributions typically follow a Gaussian profile; in this case, the experimental data (black curve) closely matches the randomized dataset (red curve), confirming the absence of Sc clustering or segregation. Together, these observations support the conclusion that the alloy retains a supersaturated solid solution with high defect density because of the additive manufacturing process.

In the W- specimen, no Sc-containing precipitates were observed in the microstructure, despite the presence of 0.3 at. % Sc in the alloy. This result is notable because according to the Al–Sc binary phase diagram, this Sc content is higher than the equilibrium solubility limit (~0.23 % at the eutectic temperature), which is sufficient for the formation of Al_3Sc precipitates under conventional processing conditions [37]. This finding can be explained by the unique thermal conditions of the WAAM process, particularly the repeated thermal cycling followed by fast cooling. These conditions influence the microstructure in several ways that collectively prevent the formation of Al_3Sc precipitates. First, the limited thermal exposure restricts atomic diffusion, making it difficult for Sc atoms to nucleate and grow into precipitates [11,38,39]. Second, the short dwell times at elevated temperatures, as shown in our previous study [14], are insufficient to activate precipitation kinetics, resulting in a retained solid solution. Third, the fast cooling induces lattice expansion, which increases the solubility limit of Sc in the Al matrix, further stabilizing the supersaturated solid solution (Fig. 2d).

For P-W specimen, after the WAAM process, the aluminum alloy specimens were aged at 300 ± 5 °C for 2 h, leading to the formation of spherical precipitates (Fig. 3). Comparison of the TEM images in Fig. 2a and 3a show that ageing eliminates many dislocations and introduces a small population of fine particles. Because the alloy's Mg content is below the critical threshold for β-phase formation in the Al–Mg phase diagram [34], β-phase particles are not expected in the matrix even in nano-scale as can be seen in the observation corroborated by the 3D-APT and reconstructions of Mg and Sc in Fig. 3d. Fig. 3e further reveals that the Mg concentration inside the particles is low and that the chemical composition of particles matches Al_3Sc. Although the precipitate number density and size are relatively small, Fig. 2f demonstrates that a fraction of Sc atoms exhibit significantly shorter nearest-neighbor (d-pair) distances than those in a random solid solution, indicating pronounced spatial correlation (see arrow in Fig. 3f) and presence of Al_3Sc particles in matrix.

Integrating established theory, literature, and our observations, the ageing sequence can be summarized as follows: During aging, the microstructural evolution is governed by the dislocation recovery and precipitation [40]. In the microstructures containing a high density of dislocations and vacancies, typical of the WAAM process [11,41], the

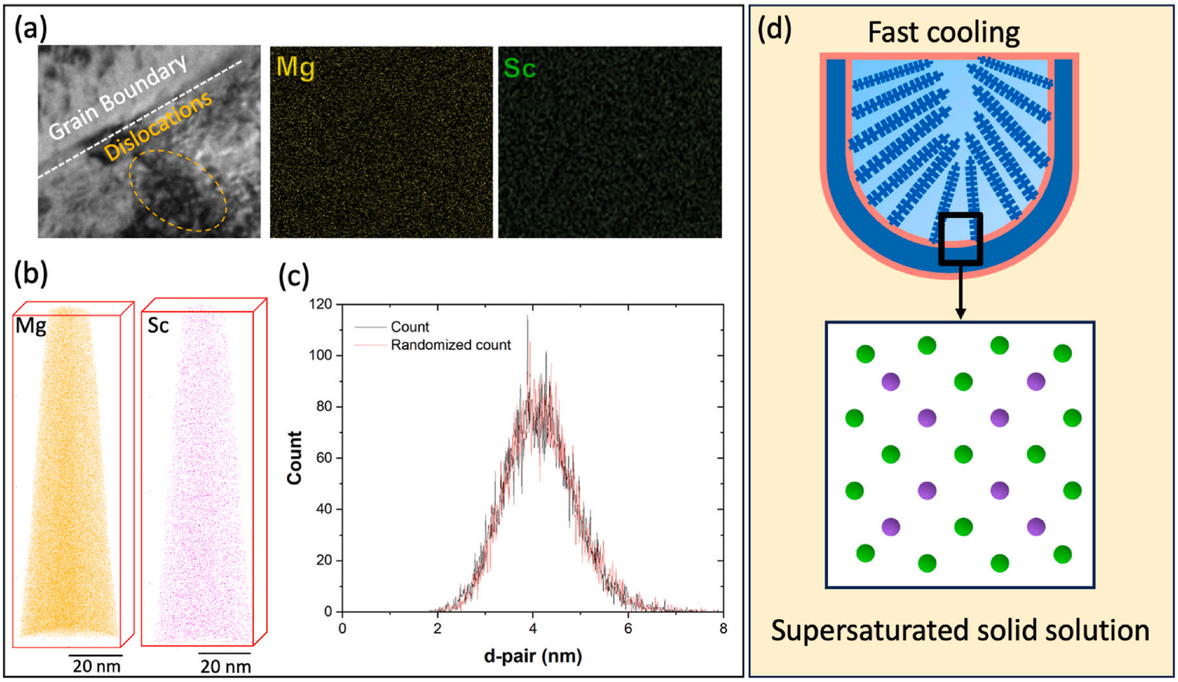

Fig. 2. (a) Representative bright-field TEM image and corresponding EDS elemental maps showing the microstructure and distribution of Mg and Sc in the as-built WAAM specimen. (b) 3D APT reconstruction revealing a homogeneous distribution of alloying elements. (c) Atom pair correlation analysis indicates no clustering or segregation of Sc atoms, consistent with a random solid solution. (d) Schematic representation highlighting the formation of a supersaturated solid solution because of rapid cooling in the WAAM process.

high-temperature aging process includes recovery mechanisms, such as dislocation annihilation and a reduction in dislocation density, in addition to precipitation [42]. This outcome is evident in Fig. 3a, which shows a noticeably lower dislocation density after aging. As the aging progresses, solute-like Sc-atoms begin to diffuse through the aluminum matrix and nucleate coherent Al_3Sc precipitates, often using remaining dislocations and subgrain boundaries as favorable nucleation sites [41]. This occurred because the rapid solidification during WAAM created a supersaturated solid solution of Sc in the aluminum matrix, as shown in Fig. 2. Then, thermal activation during aging allowed solutes like Sc atoms to further diffuse and react with aluminum, resulting in the growth of second phase particles. These precipitates generally exhibit a spherical shape to minimize interfacial energy and maintain coherency with the aluminum lattice [43,44]. In some regions, we observed misfit dislocations at the particle–matrix interfaces (Fig. 3b and c), indicating partial loss of coherency due to lattice mismatch, and the nature of the particles is semi- or semi-coherent.

Although precipitation and recovery may occur concurrently, previous studies indicate that recovery tends to initiate slightly earlier due to its lower activation energy [37,45]. For example, Røyset and Ryum [37] reported that Al_3Sc particles preferentially nucleate at dislocations, but recovery begins before the onset of detectable precipitation. This sequence is further supported by our DSC results, presented in the following section, which clearly show that recovery precedes the onset of Al_3Sc precipitation during aging. Therefore, the notable dislocation density decrease can be seen in the specimen, while the particle growth was not significant.

Fig. 4 illustrates the microstructure that forms during WAAM, followed directly by inter-pass rolling in the Check specimen label; likely HR-W specimen, without any subsequent heat treatment. Dark-field TEM (Fig. 4a) picks out the formation of the ellipsoidal Al_3Sc precipitates embedded in the matrix. HR-TEM (Fig. 4b) shows lattice fringes that pass seamlessly from matrix to precipitate, confirming the cube-on-cube orientation relationship, and the filtered IFFT image (4d) reveals no interfacial contrast anomalies, evidence that these ellipsoidal particles are fully coherent and free of misfit dislocations. A 3D-APT reconstruction (Fig. 4e) depicts just a handful of high-aspect-ratio Sc-rich plates in the matrix. The accompanying 1D concentration profile (Fig. 4g), taken in the direction shown in Fig. 4f, rises abruptly to ~25 at. % Sc, the stoichiometry of Al_3Sc, then drops to matrix level with only a slight Sc shoulder, signaling early solute clustering. Collectively, these observations show that the coupled thermal and mechanical cycling of WAAM + rolling drives the development of large, coherent, plate-shaped Al_3Sc precipitates, in sharp contrast to the finer, semi-coherent, spheroidal particles produced in the P-W condition.

The equilibrium shape of Al_3Sc precipitates is governed by the minimization of both interfacial and elastic strain energies, with their relative importance assessed using the L parameter introduced by Thompson et al. [46]. This parameter is defined as $L = \frac{e^2 C_{44} l}{\gamma}$, where e is the misfit strain between the precipitate and the matrix, C_{44} is the elastic shear modulus of the matrix, l is the precipitate size, and γ is the interfacial energy. For the Al/Al_3Sc system, using typical values such as $e = 0.0125$, $C_{44} = 28.5$ GPa, and $l = 5$ nm [47], the calculated L value is approximately 0.1. This low value indicates that interfacial energy dominates the shape evolution rather than elastic strain energy. Wulff constructions using interfacial energies obtained by Hyland et al. [47] and Asta et al. [48] for Al_3Sc particles predict that Al_3Sc precipitates adopt faceted shapes dominated by {100}, {110}, and {111} planes, forming a complex equilibrium morphology known as the Great Rhombicuboctahedron. Our results obtained by HR-TEM, shown in Fig. 3b, confirm these predictions, with dominant {110} facets and visible {100} facets observed in the aged Al_3Sc precipitates. However, our investigations using APT and HR-TEM (Fig. 4) show that there are fewer visible facets in the particles observed in the HR-W specimen. This suggests that the shape of precipitates in HR-W specimen cannot be reliably predicted using current knowledge and models. Further investigation is needed to understand this behavior, and this will be discussed in more detail in Section 4.

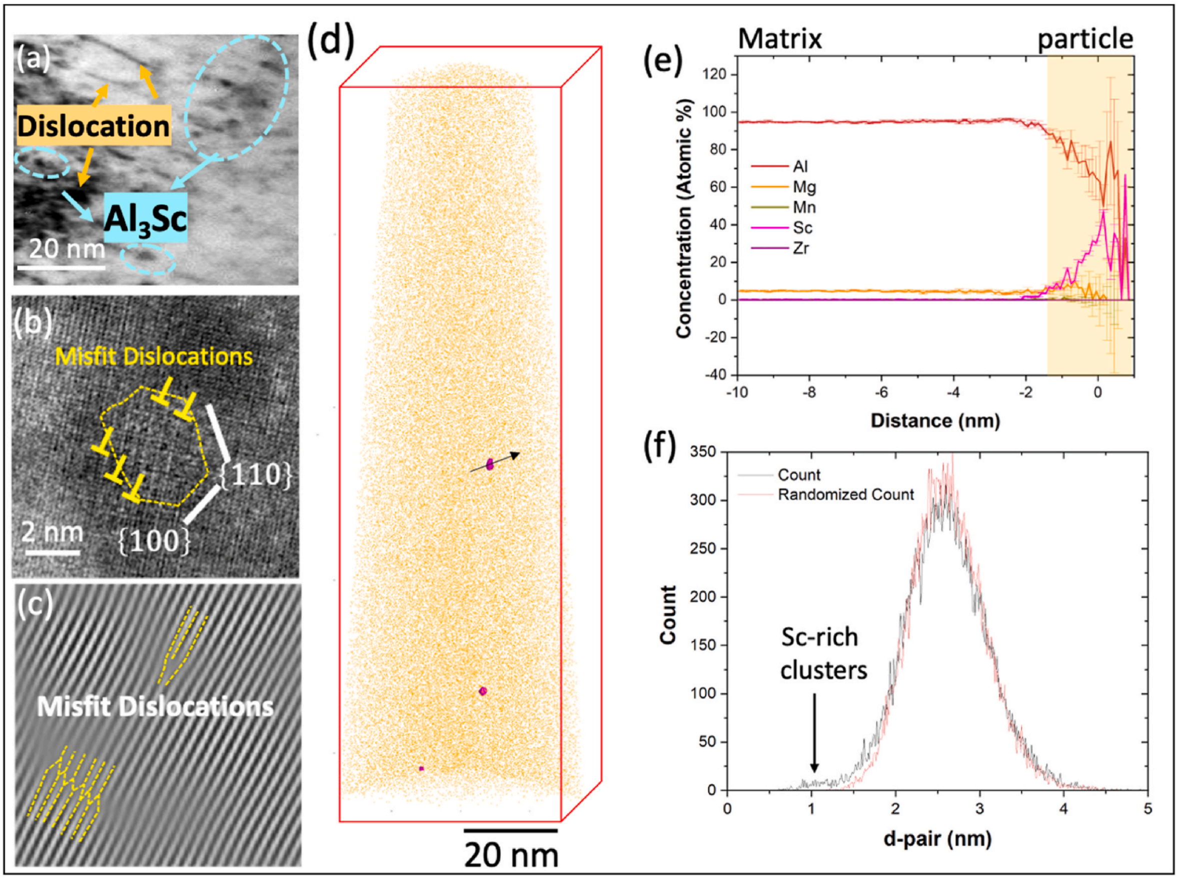

Fig. 3. (a) Bright-field TEM micrograph of the WAAM-fabricated alloy aged at 300 ± 5 °C for 2 h, (b) HR-TEM image of a representative Al_3Sc precipitate, and (c) inverse fast-Fourier-transform (IFFT) pattern highlights misfit dislocations at the particle–matrix interface. (d) 3D-APT reconstruction revealing the distribution of Sc-rich particles within the matrix. (e) 1D-APT concentration profile across a precipitate, confirming pronounced Sc enrichment and Mg depletion. (f) Atom-pair-correlation (d pair) analysis of the APT data, demonstrating Sc–Sc clustering.

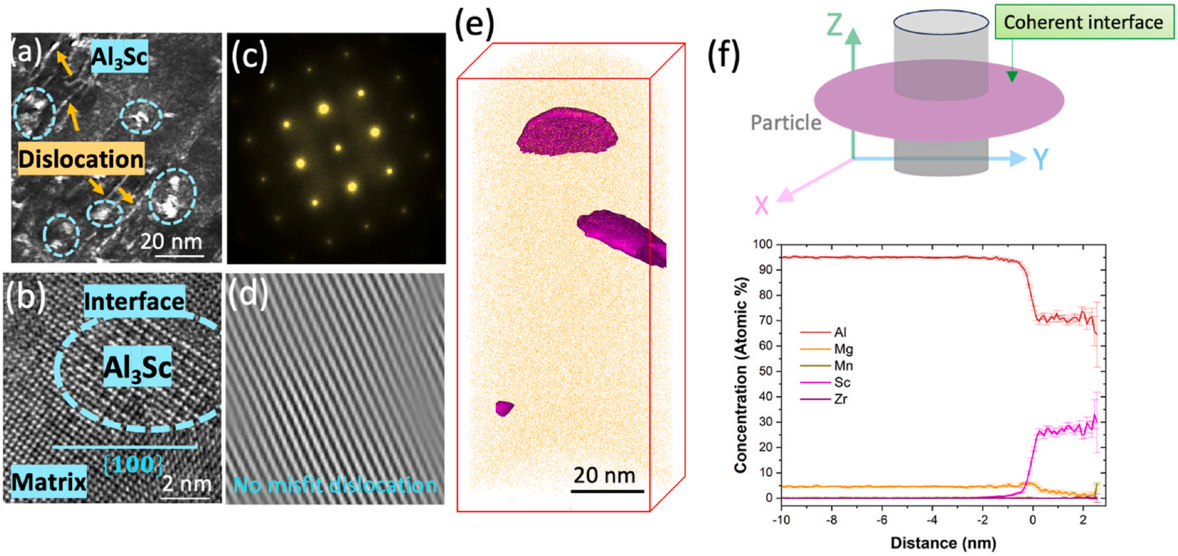

Fig. 4. (a) Dark-field TEM image, (b) HR-TEM micrograph of a representative particle; the lattice fringes continue seamlessly from matrix to precipitate, indicating a cube-on-cube orientation relationship. (c) FFT of the region in (b), (d) Inverse FFT filter of the interface, (e) 3D-APT reconstruction (orange = Mg, purple iso-surface = Sc), (f) Schematic defining the analysis direction in (g); (g) 1-D solute concentration profile normal to a particle. (For interpretation of the references to colour in this figure legend, the reader is referred to the Web version of this article.)

3.2. Hydrogen trapping in second-phase particles

To investigate the nature of hydrogen trap sites, we conducted a detailed analysis of hydrogen-charged specimens using TDS which was shown in Fig. 5. This Figure demonstrates that the two WAAM build strategies create fundamentally different hydrogen-trapping landscapes. TDS measurements show different hydrogen mapping profile in the specimens, showing four distinct desorption peaks at ~130 °C, ~348 °C, ~450 °C, and ~540 °C in the HR-W specimens (Fig. 5a), while three distinct peaks were observed for the P-W specimen. Peaks at 130 °C, 348 °C, and 540 °C are common to both builds. According to the literature, the first, second, and fourth peaks correspond to the hydrogen residing in the aluminum lattice [49–51], dislocations [51,52] and grain boundaries [23,53], respectively. The higher height of the second peak in the HR-W specimen compared to the P-W specimen can be attributed to the higher dislocation density in the HR-W specimen. The third, high-temperature peak at ~450 °C, which appears only in the HR-W specimen, indicates a population of relatively irreversible traps that release hydrogen at elevated temperatures. Because the emergence of the third peak in HR-W specimens coincides uniquely with the formation of ellipsoidal particles in this specimen (Fig. 4), Peak 3 can be attributed to hydrogen trapping in these particles. By contrast, the P-W alloy contains only small, semi-coherent and spherical Al_3Sc precipitates; the corresponding TDS spectrum lacks the 450 °C peak entirely, confirming that such particles do not provide effective deep-trapping sites.

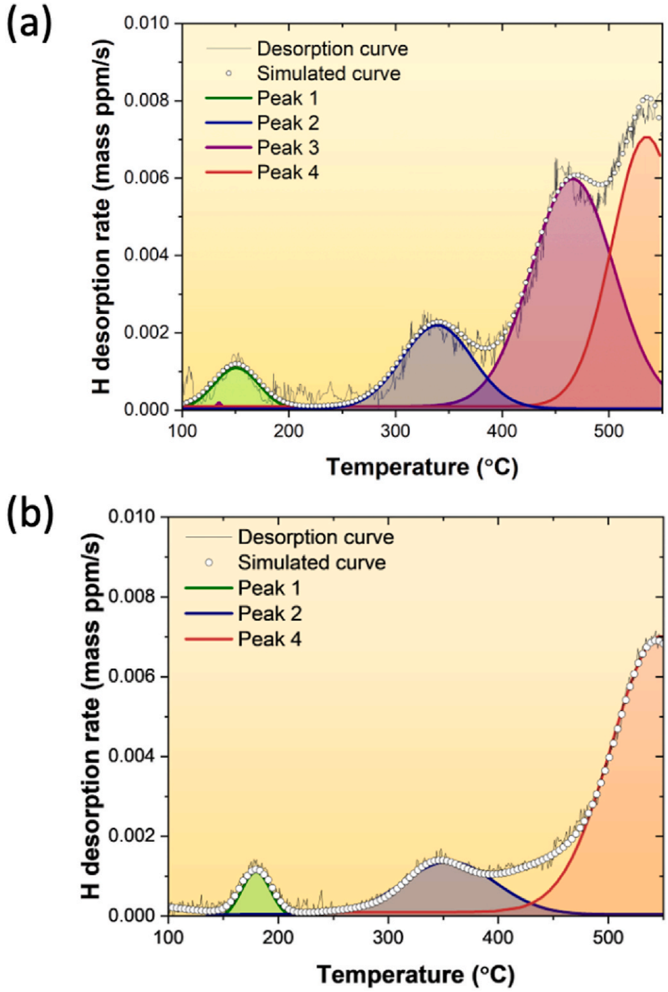

Fig. 5. TDS result for (a) HR-W and (b) P-W specimens.

4. Discussion

4.1. Effect of in-process rolling on precipitation and precipitate shape in wire arc additively manufactured specimens

4.1.1. Effect of excess vacancies

During the process, HR-W beads experience a brief but intense compressive stress (≈30 % height reduction delivered in ~5 ms at $\dot{\varepsilon} \approx 10^2\ s^{-1}$). During this pulse, according to the theory proposed by Militzer et al. [54], two vacancy sources are active, and the vacancy source term can be expressed as follows:

$$\Pi = \chi \frac{\sigma\Omega_0}{Q_f}\ \dot{\varepsilon} + \zeta \frac{C_j\Omega_0}{4b^3}\dot{\varepsilon}, \tag{1}$$

where the first (mechanical) part scales directly with the rolling stress ($\sigma \approx 100\ MPa$) and the very high strain rate, while the second (thermal-jog) part remains active because the bead temperature sits near 0.6 T_m. Ω_0, Q_f, and b are the atomic volume, vacancy formation energy and Burger's vector, respectively. The jog density (C_j) can be obtained by Eq. (2) where μ and ν are shear modulus and Poisson's ratio, respectively. The neutralization factor (ζ) represents the partial cancellation of vacancy-emitting and vacancy-absorbing jogs; $\zeta = 0.5$ means no cancellation (maximum thermal production), while $\zeta \rightarrow 0$ corresponds to perfect neutralization [55]. Because the rolling takes only a few seconds, ζ cannot evolve much below 0.5, so both terms in Eq. (1) remain significant.

$$C_j = \exp\left(-\frac{E_j}{kT}\right), E_j = \frac{\mu b^3}{4\pi(1-\nu)}, \tag{2}$$

It is known that vacancies are eliminated by diffusion to sinks, predominantly dislocations with a density of ρ and grain boundaries with spacing of L [56]. Thus, the annihilation rate can be obtained by:

$$\eta = x^2\left(D_\nu\rho + \frac{D_\nu}{L^2}\right)c_{ex}, \tag{3}$$

where D_ν is the diffusion rate of vacancies, and x is the cell-structure factor; according to the TEM image in Fig. 4a, x ≈ 16. The comparison of dislocation densities in Fig. 2a (1.12×10^{15} cm^{-2}) and Fig. 4a (1.2×10^{15} cm^{-2}) shows that there is no significant difference between the W and HR-W specimens. This might be because rolling is performed at high temperatures, which does not introduce additional dislocations; instead, dislocations are mainly generated by thermal stresses during solidification [9,10]. On the other hand, in the as-built specimen, the first term in the vacancy production equation (Eq (1)) is absent meaning that it should contain a lower vacancy concentration. Therefore, in HR-W specimen, because ρ is still close to its as-deposited value at the start of rolling, η cannot balance the suddenly huge Π. The net equation (Eq. (4)) drives a vacancy overshoot of roughly 10^2–10^3 times the equilibrium concentration in HR-W specimen (as schematically illustrated in Fig. 6a); by contrast, in as-built specimen where $\dot{\varepsilon} \approx 0$, only the weak thermal term in Eq (1) survives and dislocations or other sinks can hold the vacancy level near equilibrium. Although the arc deposition step is nominally mechanically induced strain-free, a modest vacancy flux still arises from thermally activated jog motion, solidification shrinkage and transient thermal stresses [11]. Because the macroscopic strain rate is practically zero, this source is tiny compared with Eq (1) and the existing dislocations and grain boundaries absorb the vacancies almost as soon as they form, so the un-rolled wall remains at its near-equilibrium baseline (i.e. $c_{ex} = c_{th}$) as shown schematically in Fig. 6a.

$$\frac{dc_{ex}}{dt} = \Pi - \eta \tag{4}$$

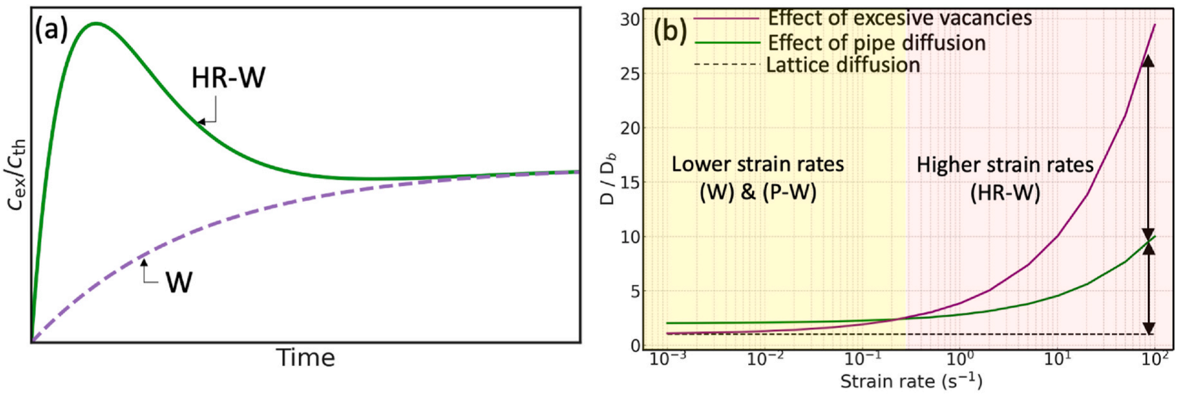

Fig. 6. (a) Schematic representation of the time dependence of the excess vacancy concentration; (b) Strain rate dependence of the enhancement factor for lattice self-diffusion in aluminum by contribution of pipe diffusion and excessive vacancies.

4.2. Effect of deformation-induced vacancies on precipitation

According to what was discussed in the previous section, excess vacancies can be generated through in-process deformation. These excess vacancies can play a critical role in further boosting diffusion rates as Armstrong et al. [57] have shown. They showed that under deformation, the excess vacancies significantly augment the effective self-diffusivity beyond what is achievable via dislocation-mediated pipe diffusion alone. In this case, self-diffusivity takes the form

$$D = D_b\left(1+\frac{c_{ex}}{c_{th}}\right)(1-g)+gD_p, \tag{5}$$

where D_b is the lattice diffusion coefficient, D_p is the pipe diffusivity, and g is the fraction of atoms associated with the pipe. Because $g \ll 1$, Eq (5) simplifies the following equation:

$$D = D_b\left(1+\frac{c_{ex}}{c_{th}}+g\frac{D_p}{D_b}\right) \tag{6}$$

The activation energy of pipe diffusion is similar to that of grain boundary diffusion, which was measured to be $Q_{gb} = 0.45$ eV in aluminum [58]. The pre-exponential factor, on the other hand, can be taken from lattice diffusion, so that it can be written as:

$$\frac{D}{D_b} = exp\left(\frac{Q-Q_{gb}}{kT}\right) \tag{7}$$

We calculated the enhancement of self-diffusion $\frac{D}{D_b}$ for steady-state conditions of deformation, i.e. $c_{ex} = c_s$ and $\rho = \rho_s$ for aluminum at 400 °C (0.6 T_m). The results were presented in Fig. 6b where the green line indicates the contribution from pipe diffusion. The results indicate that at low strain rates or when the strain rate is close to zero, the enhancement of diffusion is due to the pipe diffusion. At higher strain rates, as in the case of the HR-W specimen, the higher excess-vacancy concentration leads to significantly additional enhancement. Therefore, the appearance of second-phase particles in the HR-W specimen can be attributed to accelerated diffusion along the excessive vacancies generated by the synergistic effects of deformation-induced excess vacancies and the heat provided by additive manufacturing

In the P-W specimen, the vacancies created during deposition can be significantly annealed within the few microseconds before ageing begins. This is evident in Fig. 7a, which presents positron annihilation measurements conducted on the specimens both before ageing and after ageing for various specified durations. In aluminum alloys, positron annihilation can be resolved into three characteristic lifetime components, as illustrated in Fig. 7a and detailed in Ref. [59]. Positrons that annihilate in the defect-free aluminum matrix exhibit the shortest lifetime ($\tau_1 \leq 160$ ps). A longer lifetime ($\tau_2 \approx 215$ ps) arises when annihilation occurs inside solute clusters or coherent precipitates, while the longest one ($\tau_3 \approx 220$ ps) is associated with positrons trapped at vacancy-type defects. In the as-built W specimen and HR-W specimen, a high positron lifetime of $\geq$220 ps is observed (Fig. 7a), which indicates that a significant portion of positrons are annihilating in vacancies or vacancy-solute complexes. The higher positron lifetime in the HR-W specimen confirms the theoretical calculations, indicating a higher vacancy concentration in this specimen. Upon ageing at 300 °C for only a few seconds, the positron lifetime sharply decreases by to around 170 or 180 ps. This reduction suggests a substantial decrease in the vacancy concentration in both specimens, resulting in more positrons annihilating in the aluminum bulk, where the lifetime is approximately 160 ps. Therefore, vacancy diffusion does not play an active role in particle formation during aging. Instead, three-dimensional lattice diffusion, potentially aided by pipe diffusion along immobile dislocations (as

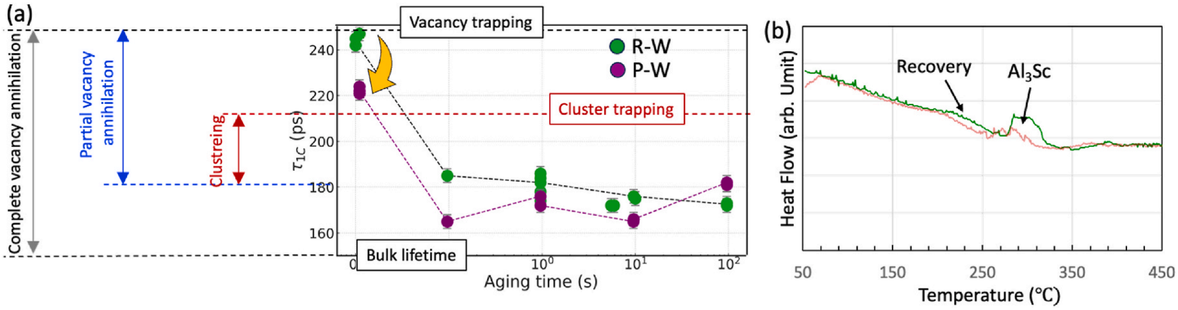

Fig. 7. (a) One-component positron lifetimes during aging of HR-W and W/P-W specimen; The arrow indicates the difference in initial vacancy concentrations between the two specimens. (b) DSC curves of the HR-W specimen (green line) and the W specimen aged for 1 s (red line) to form P-W specimen, showing the importance of excessive vacancies in formation of Al_3Sc particles. (The W specimen, after aging, is transformed into the P-W specimen). (For interpretation of the references to colour in this figure legend, the reader is referred to the Web version of this article.)

shown in Fig. 6b), may facilitate the slow migration of Sc atoms within the matrix. In this case, due to the limited diffusivity, the particles grow only a few nanometers. Because their radius surpasses the coherency limit, yet the surrounding matrix cannot elastically relax, the particles lose their lattice match early and are therefore observed as fine but semi-coherent, as observed in Fig. 2.

By contrast, the HR-W specimen undergoes intense plastic deformation, which generates a denser population of excess vacancies (Fig. 7a). These vacancies facilitate Sc diffusion via a vacancy-mediated mechanism that can be up to two orders of magnitude faster than lattice diffusion [60], while the matrix remains supersaturated (Fig. 2). As a result, Sc atoms are rapidly transported to a few energetically favorable sites, where they coalesce into ellipsoidal Al_3Sc precipitates aligned on {100} planes (Fig. 4). Vacancies indeed play a crucial role in enabling coherent interfaces [61] in HR-W specimens. They promote fast, uniform solute diffusion, which helps precipitates grow with lattice planes aligned to the matrix. In addition, vacancies assist in locally relaxing the slight misfit strain through elastic deformation of the lattice due to the growth of Al_3Sc particles, avoiding the need for dislocations [62]. Because this growth occurs while the matrix can still elastically accommodate the slight lattice misfit, the resulting precipitates remain large yet fully coherent with the Al lattice. This elastic accommodation is possible because the matrix is expected to be softened and a vacancy-rich state due to intense deformation and elevated temperature. Under these conditions, the aluminum lattice remains flexible enough to absorb the small mismatch without generating defects. The DSC data in Fig. 7b supports this interpretation. Comparing an HR-W specimen with an aged for just 1 s to intentionally remove the vacancies, the Al_3Sc formation peak is appreciably lower after the brief ageing step, indicating that eliminating excess vacancies (which was shown in Fig. 7a) suppresses further Al_3Sc precipitation. DSC also shows a peak that precedes Al_3Sc precipitation. Based on literature [63,64], this earlier peak is due to the dynamic recovery, implying that recovery is largely complete before ageing begins and that pipe diffusion contributes little to the subsequent growth of Al_3Sc particles. Thus, the dominant diffusion mechanism during precipitation, slow lattice diffusion after WAAM versus rapid vacancy-driven diffusion during deformation, determines whether the alloy ends up with a dispersion of fine, semi-coherent Al_3Sc particles or larger, coherent particles.

4.3. *Interaction of hydrogen with Al_3Sc precipitates*

To test and verify hydrogen trapping by coherent Al_3Sc particles observed by APT, we created a DFT model to probe the behavior of hydrogen at a phase boundary in a coherent $(001)Al\|(001)Al_3Sc$ bilayer; eight Al and eight Al_3Sc (001) planes were included. Hydrogen was then placed in all non-equivalent tetrahedral sites at incremental distances from the interface mid-plane, and then each configuration was fully

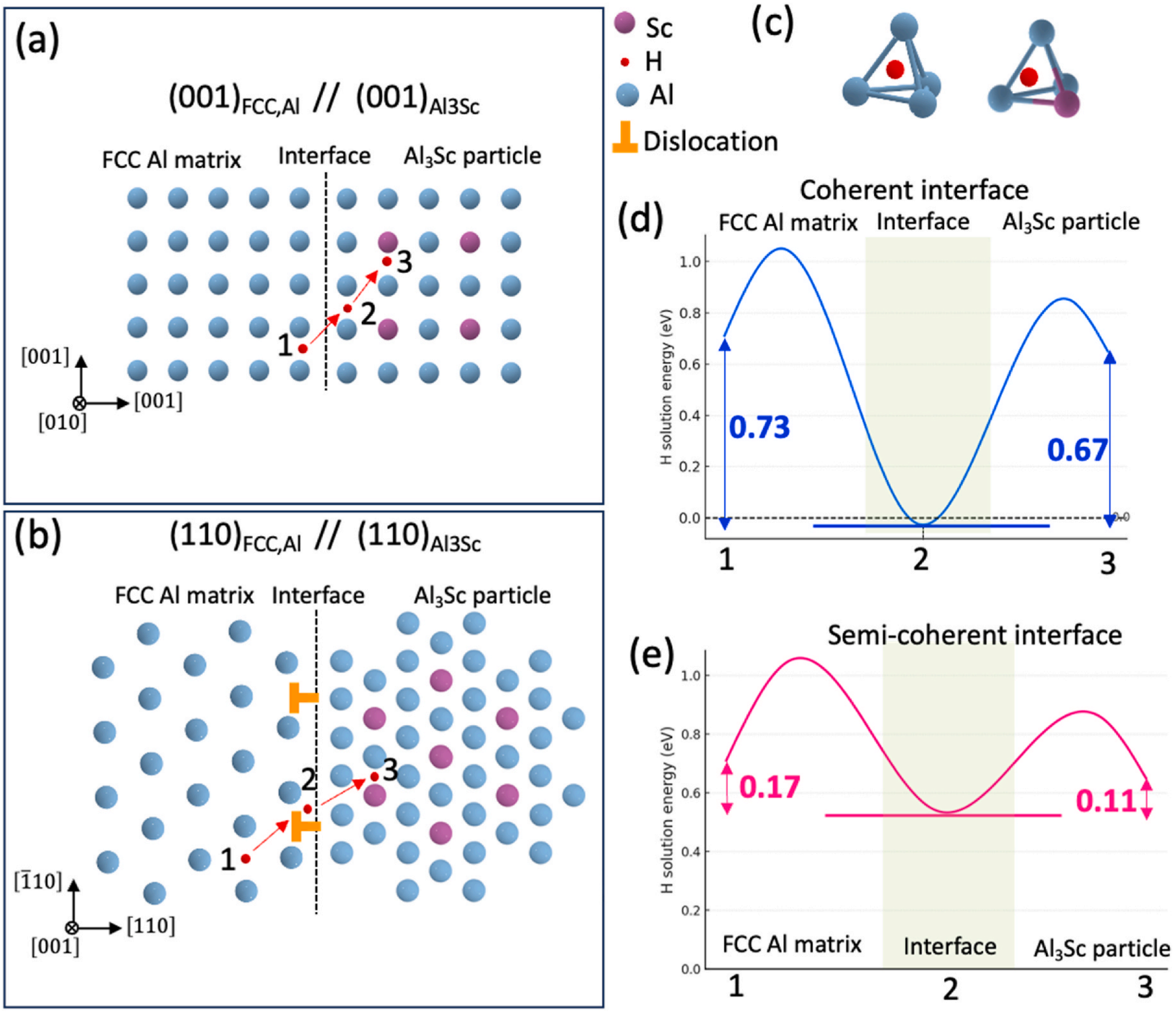

Fig. 8. Conceptual sketch of (a) coherent and (b) semi-coherent $Al_3Sc\|Al$ interfaces; (c) 3-D model of available vacancies, a hydrogen solute atom (red sphere), Al (blue spheres), Sc (purple spheres); (d) Solution energy profiles corresponding to (d) coherent and (e) semi-coherent interfaces for a hydrogen atom in the determined positions via 1-3 in (a) and (b). (For interpretation of the references to colour in this figure legend, the reader is referred to the Web version of this article.)

relaxed (as shown in Fig. 8a and b). The results indicated that when the Al_3Sc precipitate is fully coherent, the cube-on-cube lattice match imposes a 0.9 ± 0.1 % tensile hydrostatic field in the first Al layer. Inserting a single H atom into that interfacial tetrahedral site gave a solution energy (ΔE_s) of −0.02 eV (Table 3), which is about 0.7 eV lower than the +0.71 eV we obtained for bulk f. c.c. Al. This ΔE_s makes the coherent interface the most favorable location for hydrogen in the microstructure.

To model that loss of coherency, we put a semi-coherent particle in the matrix and relaxed the misfit by introducing a periodic array of ⟨110⟩ 60° dislocations. With the long-range relaxation of the tensile residual stress, the interfacial solution energy increased to 0.54 ± 0.03 eV (Table 3). This indicates that hydrogen cannot favorably dissolve at the particle–matrix interface, and the P-W specimen, dominated by semi-coherent Al_3Sc precipitates, does not provide effective hydrogen trapping sites. These calculations explain the particles formed during in process hot-rolled WAAM builds, showing better hydrogen tolerance than P-W specimens, in which the particles become semi-coherent.

The results indicate that by combining in-process hot rolling with WAM, we drive Al_3Sc away from its usual near-spherical shape into ellipsoidal precipitates that spread widely in the {001} planes yet remain fully coherent. Such flattened particles have not been reported before in Al–Sc systems. More interestingly, their low solution energy (−0.02 eV) value can be considered as one of the most favorable solution energies reported for any Al-based dispersoid system to date [49,53,65]. It provides a benchmark against which alternative dispersoids (Al_3Zr) or complex core–shell particles. This study also shows that the alloy's final properties are engineered by the coupling of additive manufacturing with an in-process thermomechanical step that injects vacancies and shapes the microstructure in real time.

5. Conclusion

We investigated the formation and hydrogen-trapping behavior of Al_3Sc precipitates in Al-1.4 Mg-0.3Sc alloy specimens fabricated by WAAM, WAAM and post-process aging, as well as in specimens produced by WAAM combined with in-process rolling, and found:

- In as-built WAAM specimens, despite the presence of 0.3 at. % Sc (higher than the solubility limit), no Al_3Sc particles form due to suppressed diffusion and elevated solubility from rapid solidification. The alloy remains a supersaturated solid solution with high defect density.
- post-processing at 300 °C for 2 h of the as-built WAAM specimens leads to the precipitation of fine, spheroidal Al_3Sc particles with semi-coherent interfaces. This is attributed to limited diffusivity governed by lattice diffusion and vacancy annihilation prior to precipitation.
- Combination of hot rolling and WAAM processing induces a high density of excess vacancies via intense in-process deformation, which dramatically enhances solute diffusivity and drives the rapid nucleation and growth of large, elongated ellipsoid Al_3Sc precipitates along {001} planes with coherent interfaces, a morphology not previously reported for this phase.
- Positron annihilation lifetime spectroscopy confirms a high vacancy concentration immediately after HR-W processing and shows rapid vacancy depletion upon artificial ageing.
- Correlative APT and TDS analyses show that only the coherent Al_3Sc precipitates act as deep hydrogen traps, evident from a distinct desorption peak at ~400 °C and localized deuterium at Sc-rich ellipsoidal particles. DFT calculations reveal a solution energy of $\Delta E \approx -0.02$ eV for H at coherent Al_3Sc/Al interfaces, compared to +0.54 eV at semi-coherent interfaces and +0.71 eV in bulk Al. This makes coherent Al_3Sc one of the most favorable hydrogen trap sites reported for Al alloys.

These findings demonstrate that coupling additive manufacturing with in-process thermomechanical rolling enables control over precipitate coherency, shape, and hydrogen interaction, offering a novel pathway to engineer hydrogen-resistant lightweight alloys through vacancy-mediated microstructure design.

Table 3
DFT-calculated hydrogen solution energies (ΔE_s) at $Al_3Sc||Al$ interfaces.

Hydrogen site	Local defect/stress state	ΔE_s (eV)
1. Coherent $Al_3Sc||Al$ interface	0.9 % tensile hydrostatic field	−0.02 ± 0.05
2. Misfit-dislocation core (semi-coherent interface)	Dilatational core, no long-range strain	0.54 ± 0.03
3. Bulk f.c.c. Al	Stress-free lattice	0.71 ± 0.05
4. Interior of Al_3Sc	~ 1 % hydrostatic compression	0.65–0.80

CRediT authorship contribution statement

Mahdieh Safyari: Writing – review & editing, Writing – original draft, Visualization, Validation, Supervision, Methodology, Investigation, Funding acquisition, Formal analysis, Data curation, Conceptualization. **Michael K. Eusterholz:** Writing – original draft, Visualization, Software, Investigation, Formal analysis. **Masoud Moshtaghi:** Writing – original draft, Visualization, Validation, Supervision, Resources, Methodology, Investigation, Funding acquisition, Formal analysis, Conceptualization.

Declaration of competing interest

The authors declare that they have no known competing financial interests or personal relationships that could have appeared to influence the work reported in this paper.

Acknowledgments

This work was carried out as part of the GrAHAM project (project number: 371311), and HyFAT (project number: 370633) funded by the Research Council of Finland. The authors would also like to acknowledge the Karlsruhe Nano Micro Facility (KNMFi) for providing access to advanced instrumentation (project number: 2024-032-032085), which significantly supported the experimental work.

Data availability

Data will be made available on request.

References

[1] T. Petkov, T. Veziroglu, J. Sheffield, An outlook of hydrogen as an automotive fuel, Int. J. Hydrogen Energy 14 (1989) 449–474, https://doi.org/10.1016/0360-3199(89)90031-1.
[2] M. Moshtaghi, M. Safyari, M.M. Khonsari, Hydrogen-enhanced entropy (HEENT): a concept for hydrogen embrittlement prediction, Int. J. Hydrogen Energy 53 (2024) 434–440, https://doi.org/10.1016/j.ijhydene.2023.12.068.
[3] M. Safyari, A. Rauscher, S. Ucsnik, M. Moshtaghi, Hydrogen trapping and permeability in carbon fiber reinforced aluminum alloys, Int. J. Hydrogen Energy 50 (2024) 199–210, https://doi.org/10.1016/j.ijhydene.2023.09.206.
[4] H. Kamoutsi, G.N. Haidemenopoulos, V. Bontozoglou, S. Pantelakis, Corrosion-induced hydrogen embrittlement in aluminum alloy 2024, Corros. Sci. 48 (2006) 1209–1224, https://doi.org/10.1016/j.corsci.2005.05.015.
[5] S. Cooke, K. Ahmadi, S. Willerth, R. Herring, Metal additive manufacturing: technology, metallurgy and modelling, J. Manuf. Process. 57 (2020) 978–1003, https://doi.org/10.1016/j.jmapro.2020.07.025.
[6] L.E. Murr, A metallographic review of 3D printing/additive manufacturing of metal and alloy products and components, Metallogr. Microstruct. Anal. 7 (2018) 103–132, https://doi.org/10.1007/s13632-018-0433-6.
[7] H.A. Dabbas, I.M. Aladwan, A. Agarwal, M. Ilunga, O. Badran, I.I. Ikhries, Comparative investigation of mechanical characteristics and microstructure in maraging steel fabricated via DMLS and CNC techniques, IJCMEM 13 (2025), https://doi.org/10.18280/ijcmem.130106.

[8] M. Gurz, E. Baltacioglu, Y. Hames, K. Kaya, The meeting of hydrogen and automotive: a review, Int. J. Hydrogen Energy 42 (2017) 23334–23346, https://doi.org/10.1016/j.ijhydene.2017.02.124.

[9] M.M. Kirka, P. Nandwana, Y. Lee, R.R. Dehoff, Solidification and solid-state transformation sciences in metals additive manufacturing, Scr. Mater. 135 (2017) 130–134, https://doi.org/10.1016/j.scriptamat.2017.01.005.

[10] M. Safyari, N. Takata, D. Kim, M.M. Khonsari, M. Moshtaghi, Effect of hydrogen on dynamic precipitation in additively manufactured aluminum alloys: evidence for HEENT mechanism, J. Alloys Compd. (2025) 180395, https://doi.org/10.1016/j.jallcom.2025.180395.

[11] Mahdieh Safyari, Fabio Haunreiter, Shogo Furuta, Pei Loon Khoo, Florian Mayrhofer, Masakazu Kobayashi, Masoud Moshtaghi, Manipulating Nanostructure during Wire Arc Additive Manufacturing Defeats Hydrogen Embrittlement, (n.d.).

[12] M. Safyari, M. Schnall, F. Haunreiter, M. Moshtaghi, Design of hydrogen embrittlement resistant 7xxx-T6 aluminum alloys based on wire arc additive manufacturing: changing nanochemistry of strengthening precipitates, Mater. Des. 243 (2024) 113030, https://doi.org/10.1016/j.matdes.2024.113030.

[13] L. Li, Q. Wang, K. Wang, W. Wang, Y. Zhang, X. Zhang, Precipitation behavior of supersaturated solid-solubility CuCrZr alloy by additive manufacturing, Mater. Sci. Eng., A 901 (2024) 146557, https://doi.org/10.1016/j.msea.2024.146557.

[14] M. Safyari, S. Furuta, P.L. Khoo, M. Kobayashi, M. Moshtaghi, Exceptional stress corrosion cracking resistance of additively manufactured aluminum alloys in simulated marine environments, Mater. Des. 254 (2025) 113924, https://doi.org/10.1016/j.matdes.2025.113924.

[15] P. Liu, Z. Wang, Y. Xiao, M.F. Horstemeyer, X. Cui, L. Chen, Insight into the mechanisms of columnar to equiaxed grain transition during metallic additive manufacturing, Addit. Manuf. 26 (2019) 22–29, https://doi.org/10.1016/j.addma.2018.12.019.

[16] M.J. Bermingham, D.H. StJohn, J. Krynen, S. Tedman-Jones, M.S. Dargusch, Promoting the columnar to equiaxed transition and grain refinement of titanium alloys during additive manufacturing, Acta Mater. 168 (2019) 261–274, https://doi.org/10.1016/j.actamat.2019.02.020.

[17] H.L. Wei, G.L. Knapp, T. Mukherjee, T. DebRoy, Three-dimensional grain growth during multi-layer printing of a nickel-based alloy Inconel 718, Addit. Manuf. 25 (2019) 448–459, https://doi.org/10.1016/j.addma.2018.11.028.

[18] M. Safyari, M. Ahmad, J.-N. Audinot, A. Biesemeier, M. Moshtaghi, Influence of welding-induced microstructure on fatigue crack growth in 5xxx aluminum alloys in air and hydrogen environments, Mater. Des. 260 (2025) 115220, https://doi.org/10.1016/j.matdes.2025.115220.

[19] W.J. Sames, F.A. List, S. Pannala, R.R. Dehoff, S.S. Babu, The metallurgy and processing science of metal additive manufacturing, Int. Mater. Rev. 61 (2016) 315–360, https://doi.org/10.1080/09506608.2015.1116649.

[20] P.A. Colegrove, H.E. Coules, J. Fairman, F. Martina, T. Kashoob, H. Mamash, L. D. Cozzolino, Microstructure and residual stress improvement in wire and arc additively manufactured parts through high-pressure rolling, J. Mater. Process. Technol. 213 (2013) 1782–1791, https://doi.org/10.1016/j.jmatprotec.2013.04.012.

[21] F. Martina, M.J. Roy, B.A. Szost, S. Terzi, P.A. Colegrove, S.W. Williams, P. J. Withers, J. Meyer, M. Hofmann, Residual stress of as-deposited and rolled wire+arc additive manufacturing Ti–6Al–4V components, Mater. Sci. Technol. 32 (2016) 1439–1448, https://doi.org/10.1080/02670836.2016.1142704.

[22] L. Ren, H. Gu, W. Wang, S. Wang, C. Li, Z. Wang, Y. Zhai, P. Ma, Effect of Sc content on the microstructure and properties of al–mg–sc alloys deposited by wire arc additive manufacturing, Met. Mater. Int. 27 (2021) 68–77, https://doi.org/10.1007/s12540-020-00763-0.

[23] M. Moshtaghi, M. Safyari, S. Kuramoto, T. Hojo, Unraveling the effect of dislocations and deformation-induced boundaries on environmental hydrogen embrittlement behavior of a cold-rolled Al–Zn–Mg–Cu alloy, Int. J. Hydrogen Energy 46 (2021) 8285–8299, https://doi.org/10.1016/j.ijhydene.2020.12.028.

[24] M. Safyari, M. Moshtaghi, S. Kuramoto, On the role of traps in the microstructural control of environmental hydrogen embrittlement of a 7xxx series aluminum alloy, J. Alloys Compd. 855 (2021) 157300, https://doi.org/10.1016/j.jallcom.2020.157300.

[25] M. Safyari, M. Moshtaghi, S. Kuramoto, Environmental hydrogen embrittlement associated with decohesion and void formation at soluble coarse particles in a cold-rolled Al–Cu based alloy, Mater. Sci. Eng., A 799 (2021) 139850, https://doi.org/10.1016/j.msea.2020.139850.

[26] M. Safyari, M. Moshtaghi, S. Kuramoto, Effect of strain rate on environmental hydrogen embrittlement susceptibility of a severely cold-rolled Al–Cu alloy, Vacuum 172 (2020) 109057, https://doi.org/10.1016/j.vacuum.2019.109057.

[27] M. Safyari, M. Moshtaghi, S. Kuramoto, T. Hojo, Influence of microstructure-driven hydrogen distribution on environmental hydrogen embrittlement of an Al–Cu–Mg alloy, Int. J. Hydrogen Energy 46 (2021) 37502–37508, https://doi.org/10.1016/j.ijhydene.2021.09.013.

[28] M. Safyari, N. Khossossi, T. Meisel, P. Dey, T. Prohaska, M. Moshtaghi, New insights into hydrogen trapping and embrittlement in high strength aluminum alloys, Corros. Sci. 223 (2023) 111453, https://doi.org/10.1016/j.corsci.2023.111453.

[29] M. Moshtaghi, E. Maawad, A. Bendo, A. Krause, J. Todt, J. Keckes, M. Safyari, Design of high-strength martensitic steels by novel mixed-metal nanoprecipitates for high toughness and suppressed hydrogen embrittlement, Mater. Des. 234 (2023) 112323, https://doi.org/10.1016/j.matdes.2023.112323.

[30] M. Safyari, M. Moshtaghi, Dependence of the mechanical properties of a metastable austenitic stainless steel in high-pressure hydrogen gas on machining-induced defects, Mater. Lett. 340 (2023) 134149, https://doi.org/10.1016/j.matlet.2023.134149.

[31] M. Moshtaghi, M. Safyari, Different augmentations of absorbed hydrogen under elastic straining in high-pressure gaseous hydrogen environment by as-quenched and as-tempered martensitic steels: combined experimental and simulation study, Int. J. Hydrogen Energy 48 (2023) 27408–27415, https://doi.org/10.1016/j.ijhydene.2023.03.396.

[32] M. Safyari, M. Moshtaghi, Welding design of API 5L X65 pipeline steel: effects of robotic hybrid laser arc welding versus GMAW on fracture toughness evaluated by SENT tests in air and hydrogen, Mater. Des. 254 (2025) 113950, https://doi.org/10.1016/j.matdes.2025.113950.

[33] M. Safyari, S. Bhosale, M. Moshtaghi, Capacity of hydrogen traps affects H-assisted crack initiation and propagation mechanisms in martensitic steels, Eng. Fail. Anal. 163 (2024) 108560, https://doi.org/10.1016/j.engfailanal.2024.108560.

[34] N.C. Goel, J.R. Cahoon, B. Mikkelsen, An experimental technique for the rapid determination of binary phase diagrams: the Al-Mg system, Metall. Trans. A 20 (1989) 197–203, https://doi.org/10.1007/bf02670245.

[35] M. Moshtaghi, M. Safyari, G. Mori, Combined thermal desorption spectroscopy, hydrogen visualization, HRTEM and EBSD investigation of a Ni–Fe–Cr alloy: the role of hydrogen trapping behavior in hydrogen-assisted fracture, Mater. Sci. Eng., A 848 (2022) 143428, https://doi.org/10.1016/j.msea.2022.143428.

[36] J. Zhang, C. Li, X. Yang, D. Wang, W. Hu, X. Di, J. Zhang, In-situ heat treatment (IHT) wire arc additive manufacturing of Inconel625-HSLA steel functionally graded material, Mater. Lett. 330 (2023) 133326, https://doi.org/10.1016/j.matlet.2022.133326.

[37] J. Røyset, N. Ryum, Scandium in aluminium alloys, Int. Mater. Rev. 50 (2005) 19–44, https://doi.org/10.1179/174328005X14311.

[38] D.N. Seidman, E.A. Marquis, D.C. Dunand, Precipitation strengthening at ambient and elevated temperatures of heat-treatable Al(Sc) alloys, Acta Mater. 50 (2002) 4021–4035, https://doi.org/10.1016/S1359-6454(02)00201-X.

[39] C.B. Fuller, D.N. Seidman, D.C. Dunand, Mechanical properties of Al(Sc,Zr) alloys at ambient and elevated temperatures, Acta Mater. 51 (2003) 4803–4814, https://doi.org/10.1016/S1359-6454(03)00320-3.

[40] Y. Lu, J. Wang, X. Li, Y. Chen, D. Zhou, G. Zhou, W. Xu, Effect of pre-deformation on the microstructures and properties of 2219 aluminum alloy during aging treatment, J. Alloys Compd. 699 (2017) 1140–1145, https://doi.org/10.1016/j.jallcom.2016.12.006.

[41] Y. Zhou, S. Yin, Y. Jiang, Q. Zhou, J. Peng, Y. Yan, Wire and arc additive manufacturing fabrication of ODS-RAFM steels and preliminary evaluation on microstructures and mechanical properties, J. Nucl. Mater. 572 (2022) 154068, https://doi.org/10.1016/j.jnucmat.2022.154068.

[42] E. Cerri, P. Leo, Influence of severe plastic deformation on aging of Al–Mg–Si alloys, Mater. Sci. Eng., A 410–411 (2005) 226–229, https://doi.org/10.1016/j.msea.2005.08.135.

[43] Y.-Q. Zhao, H.-L. Jia, T. Tian, T. Gu, P.-K. Ma, J.-W. Song, M. Zha, H.-Y. Wang, Improved mechanical properties of Al-xMg-yZn-Cu alloys via optimized Mg/Zn ratio and thermomechanical processing, Mater. Sci. Eng., A 911 (2024) 146916, https://doi.org/10.1016/j.msea.2024.146916.

[44] Y. Wang, D. Freiberg, Y. Huo, W. Zhu, M. Li, R.E.A. Williams, Y. Wang, A combined simulation and experimental study of the equilibrium shapes of η' and α precipitates in Mn-containing 7xxx Al-alloys, Acta Mater. 259 (2023) 119094, https://doi.org/10.1016/j.actamat.2023.119094.

[45] Recovery and recrystallization during high temperature deformation, in: Treatise on Materials Science & Technology, Elsevier, 1975, pp. 393–493, https://doi.org/10.1016/b978-0-12-341806-7.50014-3.

[46] M.E. Thompson, C.S. Su, P.W. Voorhees, The equilibrium shape of a misfitting precipitate, Acta Metall. Mater. 42 (1994) 2107–2122, https://doi.org/10.1016/0956-7151(94)90036-1.

[47] R.W. Hyland, R.C. Stiffler, Determination of the elastic constants of polycrystalline Al3Sc, Scripta Metall. Mater. 25 (1991) 473–477, https://doi.org/10.1016/0956-716x(91)90213-k.

[48] M. Asta, S.M. Foiles, A.A. Quong, First-principles calculations of bulk and interfacial thermodynamic properties for fcc-based Al-Sc alloys, Phys. Rev. B 57 (1998) 11265–11275, https://doi.org/10.1103/physrevb.57.11265.

[49] G.A. Young, J.R. Scully, The diffusion and trapping of hydrogen in high purity aluminum, Acta Mater. 46 (1998) 6337–6349, https://doi.org/10.1016/S1359-6454(98)00333-4.

[50] M. Safyari, G. Mori, S. Ucsnik, M. Moshtaghi, Mechanisms of hydrogen absorption, trapping and release during galvanostatic anodization of high-strength aluminum alloys, J. Mater. Res. Technol. 22 (2023) 80–88, https://doi.org/10.1016/j.jmrt.2022.11.111.

[51] T. Izumi, G. Itoh, Thermal desorption spectroscopy study on the hydrogen trapping states in a pure aluminum, Mater. Trans. 52 (2011) 130–134, https://doi.org/10.2320/matertrans.L-M2010825.

[52] H. Kamoutsi, G.N. Haidemenopoulos, V. Bontozoglou, P.V. Petroyiannis, SpG. Pantelakis, Effect of prior deformation and heat treatment on the corrosion-induced hydrogen trapping in aluminium alloy 2024, Corros. Sci. 80 (2014) 139–142, https://doi.org/10.1016/j.corsci.2013.11.021.

[53] J.R. Scully, G.A. Young, S.W. Smith, 19 - hydrogen embrittlement of aluminum and aluminum-based alloys, in: R.P. Gangloff, B.P. Somerday (Eds.), Gaseous Hydrogen Embrittlement of Materials in Energy Technologies, Woodhead Publishing, 2012, pp. 707–768, https://doi.org/10.1533/9780857093899.3.707.

[54] M. Militzer, W.P. Sun, J.J. Jonas, Modelling the effect of deformation-induced vacancies on segregation and precipitation, Acta Metall. Mater. 42 (1994) 133–141, https://doi.org/10.1016/0956-7151(94)90056-6.

[55] W. Witzel, Vacancy production by thermal jogs during plastic deformation, WAA Translation From- Z. Metallkd. 64 (1973) 11.

[56] W.G. Wolfer, M. Ashkin, Diffusion of vacancies and interstitials to edge dislocations, J. Appl. Phys. 47 (1976) 791–800, https://doi.org/10.1063/1.322710.

[57] P.E. Armstrong, W.V. Green, O.D. Sherby, E.G. Zukas, Generation of vacancies in tungsten by rapid-rate deformation at elevated temperature, Acta Metall. 21 (1973) 1319–1326, https://doi.org/10.1016/0001-6160(73)90173-9.

[58] H.-U. Schreiber, B. Grabe, Electromigration measuring techniques for grain boundary diffusion activation energy in aluminum, Solid State Electron. 24 (1981) 1135–1146, https://doi.org/10.1016/0038-1101(81)90182-9.

[59] Z. Yang, J. Banhart, Natural and artificial ageing in aluminium alloys – the role of excess vacancies, Acta Mater. 215 (2021) 117014, https://doi.org/10.1016/j.actamat.2021.117014.

[60] F. Seitz, On the theory of vacancy diffusion in alloys, Phys. Rev. 74 (1948) 1513–1523, https://doi.org/10.1103/PhysRev.74.1513.

[61] M. Nastar, L.T. Belkacemi, E. Meslin, M. Loyer-Prost, Thermodynamic model for lattice point defect-mediated semi-coherent precipitation in alloys, Commun. Mater. 2 (2021) 32, https://doi.org/10.1038/s43246-021-00136-z.

[62] L. Bourgeois, Y. Zhang, Z. Zhang, Y. Chen, N.V. Medhekar, Transforming solid-state precipitates via excess vacancies, Nat. Commun. 11 (2020) 1248, https://doi.org/10.1038/s41467-020-15087-1.

[63] The release of energy during annealing of deformed metals, Proc. Roy. Soc. Lond. A 232 (1955) 252–270, https://doi.org/10.1098/rspa.1955.0216.

[64] A. Rohatgi, K.S. Vecchio, The variation of dislocation density as a function of the stacking fault energy in shock-deformed FCC materials, Mater. Sci. Eng., A 328 (2002) 256–266, https://doi.org/10.1016/s0921-5093(01)01702-6.

[65] M. Safyari, M. Moshtaghi, T. Hojo, E. Akiyama, Mechanisms of hydrogen embrittlement in high-strength aluminum alloys containing coherent or incoherent dispersoids, Corros. Sci. 194 (2022) 109895, https://doi.org/10.1016/j.corsci.2021.109895.